Nanoscale Advances

ROYAL SOCIETY OF CHEMISTRY

PAPER

View Article Online
View Journal | View Issue

Cite this: *Nanoscale Adv.*, 2023, **5**, 3671

Biomass-derived carbon deposited TiO_2 nanotube photocatalysts for enhanced hydrogen production

Shaeel Ahmed Althabaiti,[a] Zaheer Khan,[a] Maqsood Ahmad Malik, *[b] Salem Mohamed Bawaked,[a] Soad Zahir Al-Sheheri,[a] Mohamed Mokhtar,[a] Sharf Ilahi Siddiqui[c] and Katabathini Narasimharao*[a]

In this study, titanium oxide nanotubes (TiO_2NTs) were deposited on the surface of activated carbon (AC) by varying the wt% of AC. The physicochemical properties of synthesized TiO_2NTs–AC nanocomposites were analysed by various characterization techniques such as XRD, FT-IR, Raman, DRUV-vis, HR-TEM, XPS, PL, and N_2 physisorption. The FT-IR, EDX, and XPS analyses proved the existence of interaction between AC and TiO_2NTs. This study found that as the content of AC increases, the surface area and pore volume increase while the energy bandgap decreases. The TiO_2NTs–AC nanocomposite with 40% AC exhibited a surface area of 291 $m^2\ g^{-1}$, pore volume of 0.045 $cm^3\ g^{-1}$ and half pore width = 8.4 Å and had a wide band gap energy (3.15 eV). In addition, the photocatalytic application of the prepared nanocomposites for photocatalytic H_2 production was investigated. The H_2 was produced *via* photo-reforming in the presence of a sacrificial agent (methanol) under sunlight irradiation. It was found that the prepared TiO_2NTs–AC nanocomposite with 40% AC acted as an efficient photocatalyst for aqueous-methanol reforming under various optimization conditions. Approximately 18 000 μmol^{-1} hydrogen gas was produced *via* aqueous-methanol reforming under optimized conditions (catalyst dose = 100 mg, temperature = 25 °C, time = 12 hours, vol. of methanol = 20% (v/v), and pH = 7). The reusability of the TiO_2NTs–AC nanocomposite was also investigated for 5 consecutive cycles, and the results suggested only a slight decline in efficiency even after the fifth cycle. This study demonstrates the ability of an activated carbon deposited TiO_2NT catalyst to produce hydrogen effectively under sunlight.

Received 2nd April 2023
Accepted 22nd May 2023

DOI: 10.1039/d3na00211j

rsc.li/nanoscale-advances

1. Introduction

Along with increasing energy demand, the fossil fuel industry is also growing at an alarming rate. Developed industries release large amounts of emissions, such as greenhouse gases (GHGs) and other air pollutants, into the atmosphere.[1] GHG emissions mainly contain toxic gases such as CO_2, NO, NO_2, and SO_2, which are fatal for humans and the environment.[1,2] Because of this condition, many efforts are being made immediately to reduce fossil fuel production and consumption considerably, although it seems a little far from possible.[3]

At this juncture, hydrogen (H_2) is emerging as an alternative to fossil fuels, which can be used as an excellent carbon-free fuel.[4] H_2 fuel cells are presently under use for automobiles as H_2 burning with O_2 generates only water as a by-product, proving to be a better fuel option.[5,6] Although H_2 is a clean and green energy source, its production on a large industrial scale is still un-affordable.[7] The significant aspects which are considered while developing the technology for H_2 production are: (i) avoiding the generation of GHGs mainly CO_x, (ii) long-term supply, and (iii) an economically viable process.[1,2]

Thermal,[8] chemical,[9] biological,[10] electrolytic,[11] photo-electrolytic[12] and photocatalytic processes[13] have been used for H_2 production. Most of the H_2 these days is produced through the steam reforming of natural gases, such as methane, following the water gas shift process.[5,6] However, conventional H_2 production processes require high temperatures and pressure, which does not make these processes sustainable and efficient.[5] Among various processes, H_2 production *via* water splitting can be recognized as the most prominent method.[14,15] The first reported suitable technology to produce H_2 *via* water splitting was the photo-assisted electrochemical method. However, it needs sophisticated instrumentations.[15] Recently, H_2 production occurred on the surface of various semiconductors (photocatalysts) *via* water splitting under light irradiation at ambient temperature, proving to be a better and more sustainable technique.[5,16] The most commonly used photocatalyst is titanium oxide, TiO_2 (non-toxic, cheap, and chemically stable).[17] However, due to the wide band gap and fast e^-–h^+ recombination, its use could not have been practical for H_2 production.[5]

[a]*Chemistry Department, Faculty of Science, King Abdulaziz University, P.O. Box 80203, Jeddah 21589, Saudi Arabia. E-mail: nkatabathini@kau.edu.sa*

[b]*Department of Chemistry, Faculty of Natural Sciences, Jamia Millia Islamia, New Delhi, 110025, India. E-mail: mamalik@jmi.ac.in*

[c]*Department of Chemistry, Ramjas College, University of Delhi, Delhi-07, India*

Notably, the criteria to obtain an environmentally friendly and efficient photocatalyst are: (i) efficient absorption of solar light, (ii) stability under working conditions, and (iii) cost-effectiveness to split water into H_2 efficiently.[5–7] These criteria can be achieved by tuning the structure of the photocatalyst to have (a) charge carrier (e^- and h^+) separation, (b) delayed e^- and h^+ recombination and their migration to surface reactive centers, (c) correct alignment of band edges, and (d) avoiding the use of expensive raw materials,[5] although practically this seems less possible as these criteria can only be achieved by doping the photocatalyst with expensive metals such as platinum, palladium, silver, *etc.*[16,18,19] TiO_2 has also been used to produce H_2 by doping different metal species.[16] Other heterogeneous materials have also been made with TiO_2, although they also did not prove to be very relevant, as their cost was high.[20,21] It should be noted that to make the process more efficient, a sacrificial agent such as methanol, ethanol, lactic acid, *etc.*, has also been used.[5,22] Since the sacrificial agent acts as a source of protons in the water splitting process, the H_2 production rate increases substantially in the presence of the sacrificial agent.[5,23,24] Although semiconductors help produce H_2 through water splitting with sacrificial agents, low-cost and fast production rates under solar light irradiation are still rare.

It is found that the use of AC with semiconductors can be a good step.[25] AC is fairly cheap, providing a good surface that can easily be decorated with semiconductors.[26] It has also been proven from the previous literature that AC combined with semiconductors helps in charge separation (or prevention of e^- and h^+ recombination) for photocatalysts.[25–27] Therefore, the merging of AC with semiconductors can be a practical option. However, there is hardly any reported study on H_2 production by combining AC with TiO_2. Therefore, in this study TiO_2NTs–AC nanocomposites were synthesized and utilized for H_2 production under solar light with sacrificial agent, methanol. This can be a great effort for energy production. This is the first study that has not been reported before. Hence, the objectives of this study could be described as (a) synthesis of AC, (b) synthesis of TiO_2NTs, (c) synthesis of TiO_2NTs–AC, (d) characterization of TiO_2NTs–AC composites, (e) H_2 production investigation, (f) optimization of H_2 production, and (g) reusability of TiO_2NTs–AC.

2. Experimental

2.1. Chemicals

Titanium(IV) isopropoxide (TTIP) ($Ti[OCH(CH_3)_2]_4$ – 97%), sodium hydroxide (NaOH – 98%), potassium hydroxide (KOH – 99.95%), and methanol (CH_3OH – 99.9%) are analytical research grade reagents and were obtained from Sigma Aldrich, UK. The reagents were used as received. In addition, walnut shells were collected from the local market. Deionized water was used for the preparation and activity tests.

2.2. Synthesis of materials

2.2.1. Preparation of walnut shell-derived activated carbon (AC). AC was synthesized using walnut shells, a biomass as a raw material.[28] In brief, the walnut shells were cleaned and dried under sunlight and then dried in an oven at 100 °C for 10 h. Then, 100 g of walnut shells were crushed well and pulverized. The pulverized shells were taken in a silica crucible and pre-carbonized at 450 °C for 3 h in a muffle furnace. Then, the crucible was allowed to cool to room temperature to obtain a black solid. Next, the product was collected and ground well with a pestle and mortar. To activate the black carbon powder, it was treated with 12% KOH solution for 5 h at 90 °C. Then, the obtained activated carbon slurry was filtered and placed in the open air for 12 h and subsequently transferred into a silica crucible to be thermally treated at 800 °C for 3 h. Next, the AC was washed with dil. HCl (5%) and double-distilled water until the pH of the filtered solution became neutral. Finally, the washed cake was dried at 100 °C for 5 h to remove the moisture and ground into fine AC powder using a pestle and mortar.

2.2.2. Synthesis of anatase TiO_2NTs. The microwave hydrothermal method was used to produce TiO_2NTs.[29] At first, 50 mL of boiling water was used to dissolve a predetermined quantity of CTAB. To this, 90 mL of solution containing 2-propanol and TTIP was added while the mixture was being stirred for 1 hour to obtain a homogeneous suspension. To this suspension, 0.2 M NaOH solution was added dropwise to maintain pH 13. Finally, the suspension was transferred into specially designed vessels and the vessels were placed in an ETHOS microwave lab station for microwave hydrothermal treatment. The treatment was continued for 1 h at 120 °C with a microwave power of 500 W under autogenous pressure. After being filtered, the precipitate was washed repeatedly until the pH of the filtrate was near 7. Finally, the washed sample was dried in an oven at 100 °C for 4 h. After this, the substance was calcined in a muffle furnace at 450 °C for 6 h.

2.2.3. Preparation of TiO_2NTs–AC nanocomposites. To make the TiO_2NTs–AC composites, a predetermined quantity of calcined TiO_2NTs was dispersed in 25 mL of 2-propanol. A solution of 2-propanol containing 25 mL was stirred continuously while an unknown quantity of AC was mixed in. The treatment was continued for an additional 1 h after the AC dispersion was introduced to the TiO_2NT solution while it was vigorously stirred and sonicated. After being made into TiO_2-NTs–AC (Scheme 1), it was filtered and then dried in a hot air oven at a temperature of 100 °C for 5 h. Four different composites were prepared by varying the wt% of AC (10, 20, 30, and 40 wt%) over a fixed amount of prepared TiO_2NT powder.

2.3. Characterization

The crystal structures of bare TiO_2NTs, AC, and TiO_2NTs–AC were examined using X-ray diffraction (XRD) on a D8 Advance Bruker powder X-ray diffractometer at a 2θ range of 10° to 80°. A Thermo-Fisher Scientific Nicolet iS5 FT-IR spectrometer was used to investigate surface functional groups of the prepared materials. Raman spectra were measured using a micro-Raman spectrometer and an image spectrograph, STR 500 mm Focal Length Laser Raman spectrometer, with a flat field: 27 mm (W) 14 mm (H), and resolution: 1/0.6 cm^{-1}/pixel. A Thermo Scientific Evolution 220 diffuse reflectance UV-vis spectrophotometer

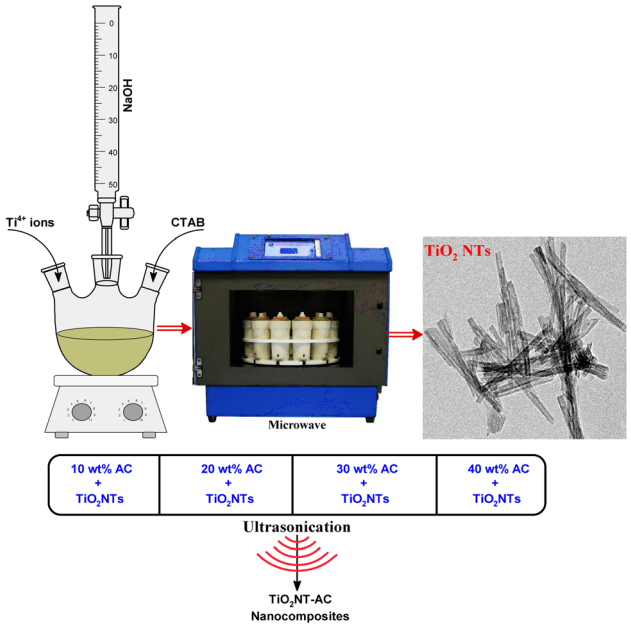

Scheme 1 Synthesis of TiO_2NTs and ultrasonic deposition of AC on TiO_2NTs.

(DR UV-vis) was used to investigate the optical properties of the as prepared materials in the wavelength range of 220–900 nm. The photoluminescence (PL) spectra were recorded at room temperature on a Varian Cary Eclipse Photoluminescence spectrophotometer. A high-resolution transmission electron microscope (HR-TEM) (FEI-TECNAI G2-20 TWIN with LaB6 filaments) working at 200 kV was used to analyse the morphologies of the produced nanomaterials. An Autosorb-iQ 2ST/MP, Quantachrome, nitrogen gas adsorption–desorption at 77 K was used to determine the specific surface areas of the synthesised materials. Using a Thermo-Scientific Escalab 250 Xi XPS apparatus with Al Kα X-rays having a spot size of 650 mm, the samples' X-ray photoelectron spectra were obtained.

2.4. Photocatalytic utilization of TiO_2NTs–AC nanocomposites

The photocatalytic reactions were performed using a laboratory build reactor equipped with a 500 W xenon lamp with a light intensity of 800 W m^{-2} and photon flux of 650 lm. A double-jacket Pyrex-glass reactor (100 mL volume) was fitted with a quartz window for UV light passage. Before starting the photocatalytic activity tests, the reactor was flushed with argon gas for 20 min. Then, the UV lamp was switched on and waited for 15 minutes to reach stability (light intensity of 45 mW cm^{-2}). The reactor is also equipped with a cold-water circulation system to keep the reaction temperature at 25 °C. To evaluate the photocatalytic efficiency of the synthesized catalysts, 20% of an aqueous methanol solution (0.15 mol methanol) and 100 mg of catalyst were used. At different time intervals, a known product sample (0.5 μL) was analysed using an Agilent gas chromatograph equipped with a TCD and Carboxen 1000 packed column.[30]

3. Results and discussion

3.1. XRD analysis

The XRD patterns of the synthesized samples are shown in Fig. 1. The X-ray diffraction patterns of AC and bare TiO_2NT samples are compared to that of the TiO_2NTs–AC NC (10–40 wt% of AC). The AC sample displayed two characteristic X-ray reflections in the XRD pattern at around 2θ values of 25° and 45° corresponding to the (002) and (101) planes that feature prominently in the cellulosic carbon framework.[31] Bare TiO_2NT samples displayed several characteristic XRD reflections for the anatase TiO_2 phase at around 26°, 38°, 47°, 54°, 56°, 62°, 68°, 69°, and 77° accounted for the (101), (004), (200), (105), (211), (204), (116), (220), and (215) planes respectively. The XRD reflections of existing TiO_2NTs matched JCPDS file (01-084-1286) of anatase TiO_2 crystals and showed good agreement with the literature.[32,33] The TiO_2NTs–AC (10–40 wt%) composite samples also showed similar XRD peaks as bare TiO_2NTs,

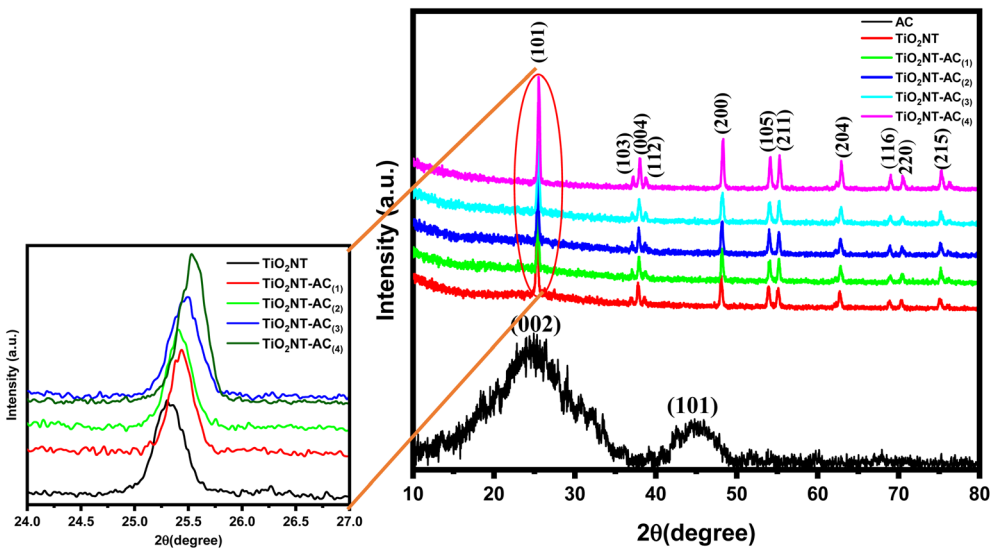

Fig. 1 XRD patterns of synthesized nanocomposites.

Table 1 The dependence of physiochemical properties of TiO_2NTs–AC at varying AC contents

Sample	TiO_2NT crystallite size (nm)	Surface area ($m^2\ g^{-1}$)	Pore volume ($cm^3\ g^{-1}$)	Half pore width (Å)	Band gap (eV)
AC	—	634	0.401	8.0	—
Pure TiO_2NTs	9.27	56	0.014	13.8	3.12
TiO_2NT–$AC_{(1)}$	6.31	127	0.020	8.4	3.08
TiO_2NT–$AC_{(2)}$	6.32	159	0.023	8.4	3.08
TiO_2NT–$AC_{(3)}$	7.49	204	0.036	8.4	3.07
TiO_2NT–$AC_{(4)}$	15.07	291	0.045	8.4	3.01

although the intensity of AC-deposited TiO_2NT samples was lower. This could be due to the excellent deposition of TiO_2NTs onto the AC through several possible interactions (electrostatic and non-electrostatic). It has also been noted that no phase change was observed, irrespective of the presence of a large amount of AC. This observation indicates the existence of highly dispersed AC over the surface of the crystalline anatase structure of TiO_2NTs.

The crystallite size was calculated using Scherrer's formula, *i.e.* $\{(D = K\lambda/\beta\cos\theta)$ where K is a constant = 0.89, λ is the wavelength of the X-ray radiation, β is the full width at half-maximum, and θ is the diffraction angle$\}$, which increases with an increase in AC contents (10 to 40 wt%). The larger crystallite size at higher AC content (40 wt%) resulted because the formation of larger-sized particles might be due to the coalescence of small grains *via* grain boundary diffusion. The change in crystallite size with an increase in AC content is presented in Table 1. Furthermore, XRD profiles did not show any reflections for other impurity phases, which suggests the high phase purity attained by the adapted synthesis method. Similar observations were reported in the previous literature.[34,35]

3.2. Raman spectroscopy

Raman spectra of the samples were obtained for a better understanding of the structure and vibrational modes of crystalline materials. The Raman spectra of TiO_2NTs and TiO_2NTs–AC (10–40 wt%) are shown in Fig. 2. The Raman spectrum of bare TiO_2NTs (see the black line) has shown three peaks at approximately 395.0, 515.0, and 635.0 cm^{-1} for $B_{1g(1)}$, A_{1g} ($+B_{1g(2)}$), and E_g, modes respectively. These peaks were related to the anatase phase of TiO_2.[28] The bands belonging to the TiO_2NTs were also observed in all the Raman spectra of TiO_2NT-deposited AC. In addition to TiO_2NT bands, two other bands were found in the Raman spectra of TiO_2NTs–AC samples (in-large inset image). These bands were assigned for the D band (sp^3-defective carbon) and G band (ordered sp^2-bonded carbon atoms) at approximately 1345.00 and ~1615.00 cm^{-1}, respectively. A slight shift in the peak position and decrease in peak intensity of the Raman peaks of TiO_2NTs–AC samples confirms the formation of TiO_2NTs–AC composites due to interaction between AC and TiO_2NTs.[34]

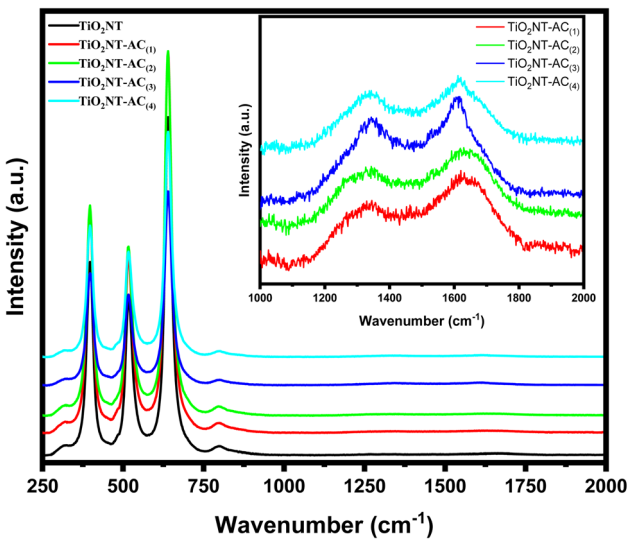

Fig. 2 Raman spectra of the prepared nanocomposites.

3.3. FT-IR spectroscopy

To investigate the functional groups present in the synthesized materials (AC, bare TiO_2NTs, and TiO_2NTs–AC) and the interaction between the functional groups (of AC and TiO_2NTs in TiO_2NTs–AC), FT-IR spectra of the samples were collected (Fig. 3). The spectrum of the bare TiO_2NT sample in the range of 4000 to 400 cm^{-1} (see the black line) shows an absorption peak at 600–500 cm^{-1} for Ti–O–Ti bond vibrations. A broad peak in the 3450–3350 cm^{-1} range was assigned to the water adsorbed on the surface of TiO_2NTs (*i.e.*, moisture). The existing AC also showed absorption peaks for the several functional groups in its FT-IR spectrum (see the red line). These were mainly assigned to the stretching frequency of hydroxyl groups (at nearly 3400 cm^{-1}), alkyls (in the range of 2900–2800 cm^{-1}), carbonyls (at 1710 cm^{-1}), amides (at near 1650 cm^{-1}), and some other groups such as –C–O and C=C in the range of 1400–1000 cm^{-1}. According to previous studies, these existing functional groups in the AC can be accounted for by its carbon (cellulosic) surface. Notably, the cellulosic surface could act as a host to accommodate the hydroxylated TiO_2NTs; thus, the TiO_2NTs–AC nanocomposites were formed due to strong interaction between the AC and TiO_2NTs. The interaction between the AC and TiO_2NTs can be observed in the FT-IR spectra of the prepared NCs. The FT-IR spectra of NCs have shown all the corresponding peaks of unmodified AC and bare TiO_2NTs, along with slight shifting in their peak positions. Peak intensities were also found to be reduced in the nanocomposites. The shift in the peak positions and decrease in the intensity of IR absorption peaks are due to the interaction between

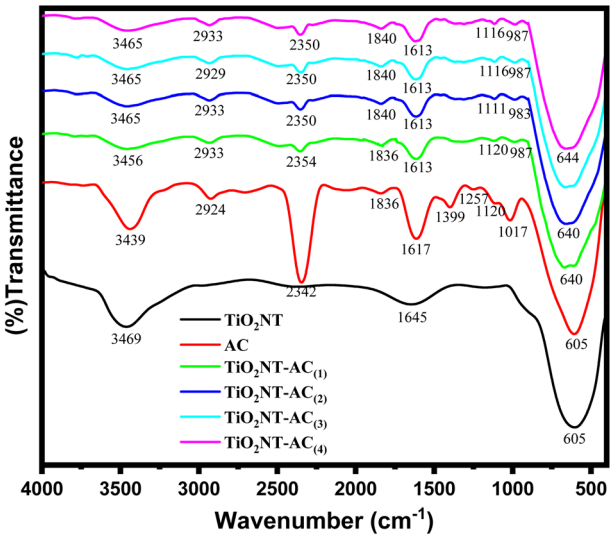

Fig. 3 FTIR spectra of the prepared nanocomposites.

the AC and TiO_2NTs *via* –OH functional groups. These observations suggest that the preparation of TiO_2NTs–AC nanocomposites is successful. The strength of the interaction of TiO_2NTs with AC increases with an increase in wt% of AC, which can also be confirmed by the lowering of peak intensities in their respective FT-IR spectra (20–40 wt% of AC). These results are in good agreement with previously reported research.[34,35]

3.4. DR UV-vis spectroscopy

The solid-state diffuse reflectance UV-visible (DR UV-vis) spectra of the samples are shown in Fig. 4a. The spectrum of the bare TiO_2NT sample showed a characteristic absorbance at around 320–420 nm corresponding to the absorption edge at around 380 nm. On the other hand the TiO_2NTs–AC nanocomposite spectra showed two absorbance peaks centered at around 230 nm and 390 nm. This could be due to the effect of the presence of activated carbon species, which would absorb both UV and visible light. The TiO_2NTs–AC composites showed extended light absorption compared with the bare TiO_2NT sample. The absorption edges of TiO_2NTs–$AC_{(1)}$, TiO_2NTs–$AC_{(2)}$, TiO_2NTs–$AC_{(3)}$ and TiO_2NTs–$AC_{(4)}$ are found to be 428, 426, 422, and 415 nm respectively. The extended absorption for the synthesized composite samples is due to strong chemical interaction between the AC and TiO_2NTs. The bandgap energy of semiconducting materials plays an important role in photocatalytic applications. Narrow energy bandgap materials may be involved in light absorption's electronic excitation (valence bands to conduction bands). These excitations lead to hole formation and free electrons that reach the catalytic surface and are responsible for the photocatalytic properties. The bandgap energy can be tuned by altering the orientation of materials. In this study, the energy bandgap was measured for bare TiO_2NTs and TiO_2NTs–AC (10–40 wt%) samples using the data obtained from DR UV-vis analysis. The Tauc plots for the synthesized samples are shown in Fig. 4b–f. It was found that the energy bandgap of TiO_2NTs decreased slightly with an increase in AC wt%, although the difference was found to be small. This is possibly due to the fact that there is no change in the crystal structure irrespective of deposition of AC on the surface of TiO_2NTs. The lowest bandgap (with a slight difference) was found for the highest content of AC in TiO_2NTs (TiO_2NTs–AC (wt% 40)) (Table 1).

3.5. Photoluminescence (PL) spectroscopy

To clarify the migration and separation effectiveness of photogenerated charge carriers at the TiO_2NTs–AC nanocomposite interface, photoluminescence (PL) spectra were obtained. The semiconductors' electron–hole (e^-–h^+) recombination is what causes the PL emission.[36] As a result, it is believed that the e^-–h^+ recombination rate is directly proportional to the PL intensity. A lower PL intensity indicates a lower e^-–h^+ recombination rate, indicating the examined photocatalyst's usefulness for photocatalytic processes.[36] Fig. 5 displays the PL spectra for the TiO_2NTs, TiO_2NTs–AC (wt% = 10), and TiO_2NTs–AC (wt% = 40) samples. In the visible range, the samples showed PL emission. The TiO_2NT sample exhibits a higher PL intensity than the TiO_2NTs–AC sample, as shown in Fig. 5. With an increase in the contents of AC (10 to 40% wt%), this intensity falls even further. Thus, it can be concluded that the e^-–h^+ recombination rate lowers noticeably as the AC content increases, most likely because of the synergistic interaction between the AC and TiO_2NTs. This finding suggests that TiO_2NTs–AC could exhibit better photocatalytic performance than pure TiO_2NTs in the future. Additionally, the PL spectra offer compelling proof of the interaction between TiO_2NTs and AC.[34]

3.6. HRTEM analysis

The HRTEM image (Fig. 6a) analysis revealed the development of bare anatase TiO_2NTs of various sizes (Table 1). The nanotubes have outer diameter around 5 and 7 nm and are 100–150 nm in length. The walls of the bare TiO_2NTs consist of 2 or 3 layers with an interlayer distance of 0.6 nm. The HRTEM image (Fig. 6c) of TiO_2NTs–AC suggested the presence of carbon on the surface of TiO_2NTs. The size of TiO_2NTs in TiO_2NTs–AC was smaller than that of bare TiO_2NTs, and breaking of the tubes into smaller ones could be observed. The lowering in the size of nanotubes could be due to the sonication treatment. The size of the tubes measured using TEM analysis is in agreement with the crystallite size calculated from the XRD analysis.

3.7. XPS analysis

XPS is one of the most advanced techniques to determine the elements constituting the sample surface, its composition, and its chemical bonding state by analysing the energy of photoelectrons released upon X-ray interactions with the analysed sample. The existing sample was also subjected to the XPS analysis. The binding energy peak profile (high-resolution XPS spectrum) of the prepared sample is shown in Fig. 7. Single region binding energy profiles (such as C 1s, Ti 2p, and O 1s) for the TiO_2NTs–AC nanocomposite sample are shown in Fig. 7e–g. The critical energy profile of Ti ions is shown in Fig. 7e. Fig. 7e displays the two dominant peaks at 457.2 eV and 462.9 eV

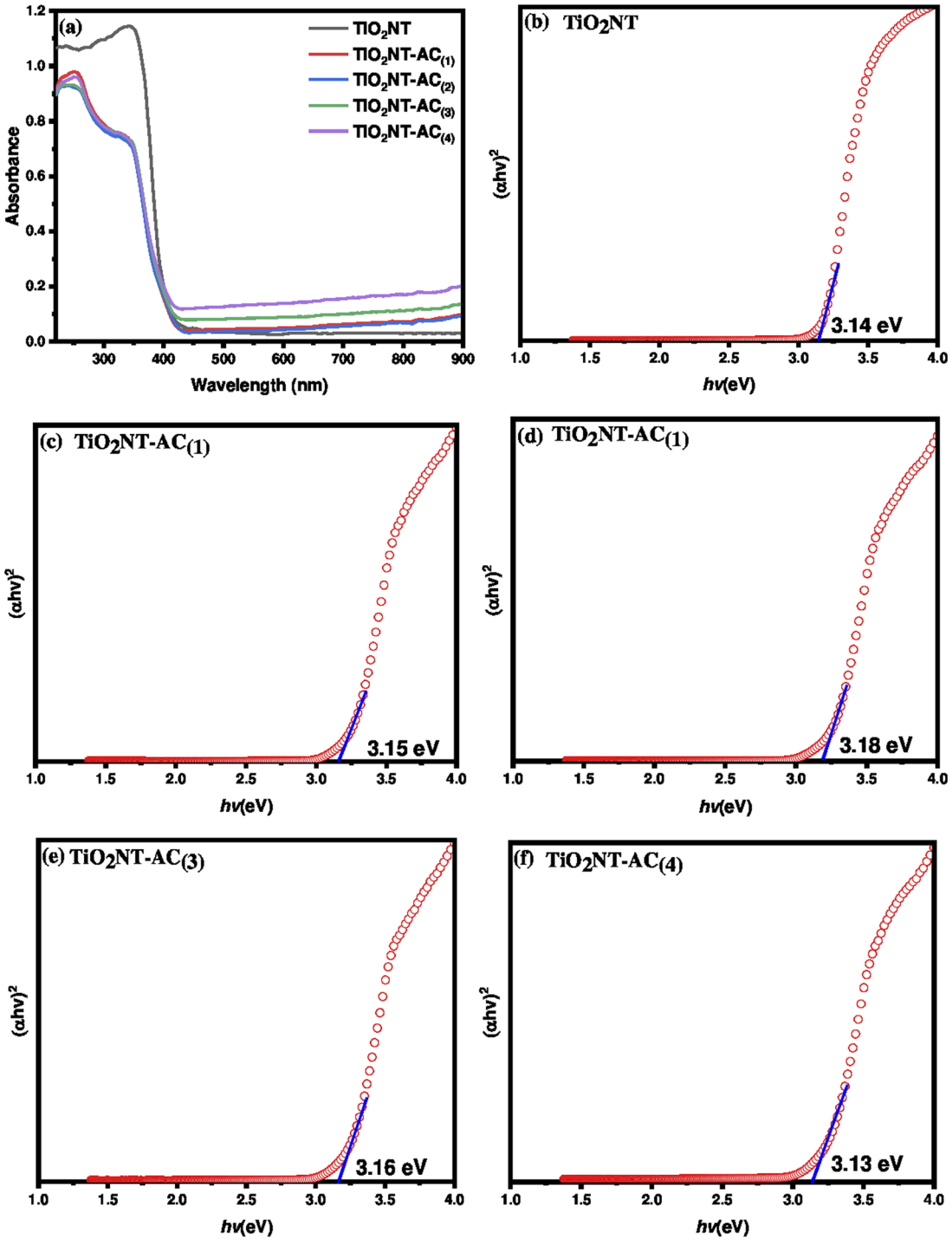

Fig. 4 (a) UV-visible diffuse reflectance spectra of pure TiO_2NT and TiO_2NT–AC nanocomposites and (b–f) results of the Tauc plot method for band gap calculation: (b) pure TiO_2NT, (c) TiO_2NT–$AC_{(1)}$, (d) TiO_2NT–$AC_{(2)}$, (e) TiO_2NT–$AC_{(3)}$, and (f) TiO_2NT–$AC_{(4)}$.

belonging to the Ti 2p doublets (Ti $2p_{3/2}$ and Ti $2p_{1/2}$). These doublets accounted for Ti ions' +4-oxidation state.[5] Notably, the Ti $2p_{3/2}$ binding energy peak of bare TiO_2NTs was assigned at 458.0 and 463.7 eV (Fig. 7c). Therefore, the shifting in the Ti $2p_{3/2}$ peak was observed in the XPS spectrum of prepared TiO_2NTs–AC.

Fig. 7f displays the binding peak at 530.5 eV for the O 1s region (lattice oxygen) related to the TiO_2NTs in the nanocomposites. It is found that the O 1s region binding energy peaks of AC (533.5 eV in Fig. 7b) and bare TiO_2NTs (528.0 eV in Fig. 9d) were assigned in slightly different ranges (Fig. 7d), suggesting the shifting in the O 1s peak in the XPS spectrum of prepared TiO_2NTs–AC.[34] Fig. 7g displays the C1 region profile related to the AC in the nanocomposites. A binding energy peak at 284.0 eV is attributed to the carbon surface.[34] It should be noted that the C1 region profile related to the NC (Fig. 7g) displayed a slight difference from the C1 region profile related to

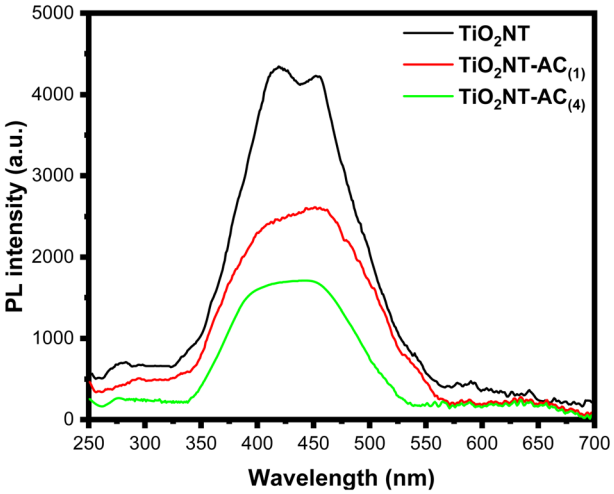

Fig. 5 Photoluminescence spectra of pure TiO_2NT, TiO_2NT–$AC_{(1)}$, and TiO_2NT–$AC_{(4)}$.

the AC (Fig. 7a). These analyses, along with the shifting in the peaks, suggested the preparation of TiO_2NTs–AC *via* interaction between the AC and TiO_2NTs.

3.8. Nitrogen gas physisorption studies

The textural properties of the prepared TiO_2NTs–AC were investigated using N_2 physisorption analysis (Fig. 8). The N_2 adsorption–desorption isotherms for TiO_2NTs–AC adopt a type-III isotherm with an apparent H_3 hysteresis loop as per IUPAC classification.[34] The type-III adsorption–desorption isotherm reflects the adsorbate's interaction with the adsorbent's surface. The observed H_3 hysteresis reflects N_2 adsorption due to the capillary condensation, possibly due to the uneven distribution of aggregates in the sample with complex pore channels. The synthesized samples' pore size distribution (PSD) patterns were obtained using the NLDFT method. The results indicated the appearance of PSD peaks corresponding to macropores in TiO_2NTs–AC, probably due to the aggregation between particles forming large-size voids. The analysis reflected the specific surface area of TiO_2NTs–AC, which is listed in Table 1 with a pore volume and a half pore width.

3.9. Photocatalytic H_2 production over TiO_2NTs–AC nanocomposites

Photoreforming of aqueous-methanol was assessed for the H_2 production over the prepared material. This study was carried out with 100 mg of photocatalyst in pure water with methanol under uninterrupted artificial visible light irradiation for 6 h. This study shows the efficient photocatalytic properties of the prepared material. The H_2 production has been observed under different conditions such as solution (water + catalyst) pH, catalyst dosage, reaction temperature and time, and the sacrificial agent's concentration such as methanol. The photocatalytic efficiency of the composite is compared with that of bare TiO_2NTs on all parameters. As can be seen, these results are shown in Fig. 9a–f. All the figures showed that the composite nanotubes showed a better hydrogen production rate under all conditions than the bare nanotubes.

Fig. 9a clearly shows that hydrogen production increases with the increase of time. In the first 2 hours, the hydrogen production concentration was ~1000.0 and ~2300.0 μmol^{-1}, over the pure NTs and composite NTs, which increased to 4600

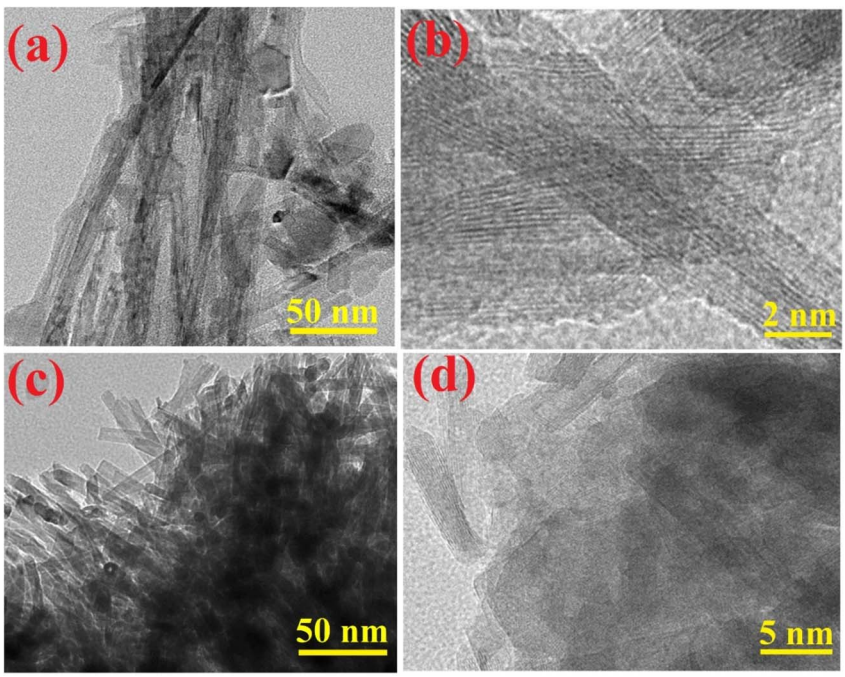

Fig. 6 TEM and HRTEM images of (a and b) pure TiO_2NT and (c and d) TiO_2NT–AC nanocomposites.

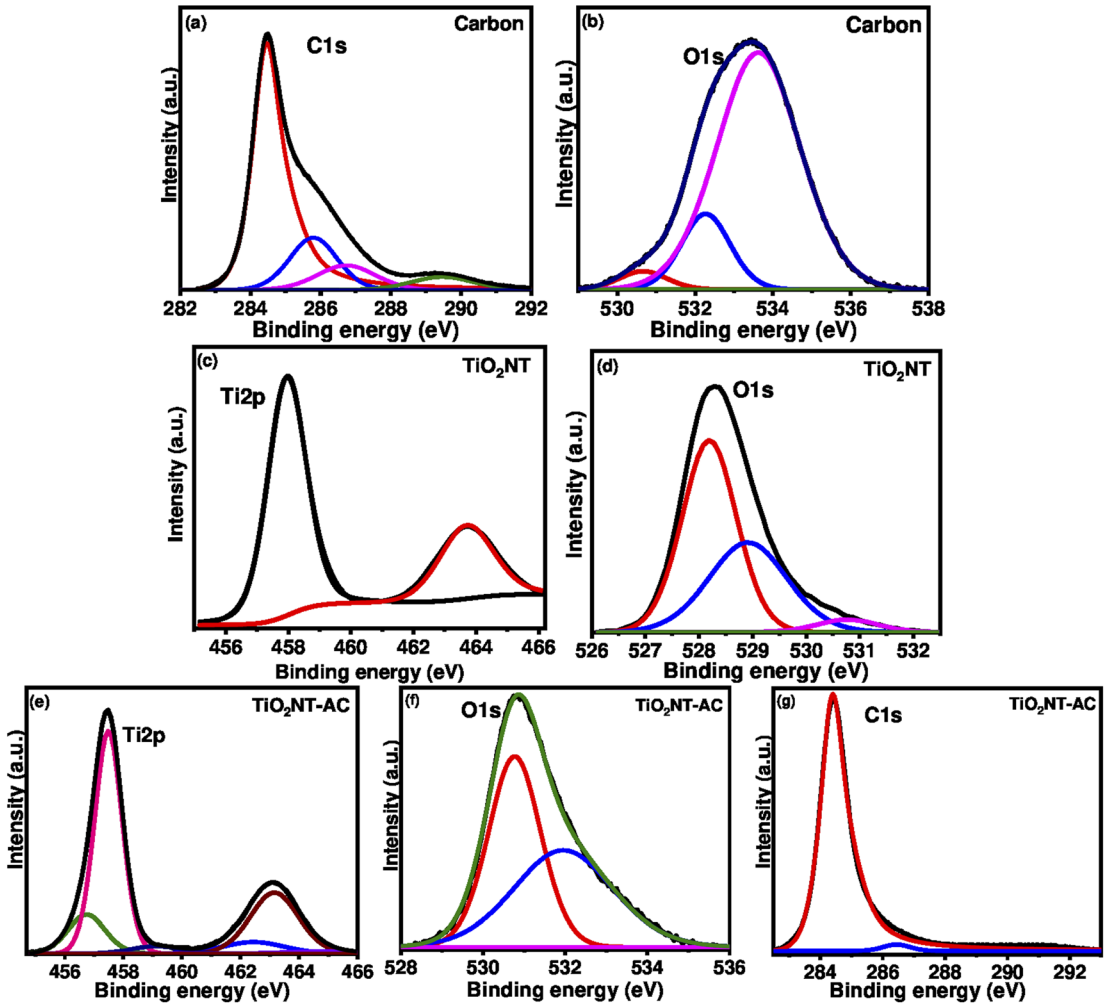

Fig. 7 Deconvoluted XPS spectra of AC, pure TiO_2NT, and TiO_2NT–AC.

and 8500 μmol^{-1} after 6 hours, respectively. On doubling the reaction time, *i.e.*, after 12 hours, this production reached 12 000 μmol^{-1} and 18 000 μmol^{-1}. It can be seen from the figure that the composite nanotubes showed much better photocatalytic properties as compared to bare TiO_2NTs. Fig. 9b clearly shows that hydrogen production increases with an increase in the concentration of sacrificial agent methanol. At vol. 5% methanol, the hydrogen production concentration was ~3100 and ~4900 μmol^{-1}, over the bare nanotubes and composite nanotubes, which increased to ~11 900 and 18 000 μmol^{-1} using 20 vol% methanol, respectively. After this, the equilibrium was attained for both materials and no efficient change was observed with a further increase in the methanol concentration. This result might be due to the surface blocking upon methanol loading, which declines the visible light absorption. Fig. 9c shows the pH effect result, which revealed that the H_2 production rate was higher at basic pH than at acidic pH. However, the best thing is that both catalysts showed the best photocatalytic activity at neutral pH (the normal pH of water). As the acidic pH was attained (towards the lower pH < 7), the hydrogen production rate decreased, and at pH = 3, the H_2 production remained at only 3460 μmol^{-1} and 8900 μmol^{-1}, over the pure and composite nanotubes, respectively. These rates increased with an increase in the pH and, at pH 7, reached 11 940 and 17 780 μmol^{-1}, which was much higher than that of acidic pH. On further increasing pH (towards the higher pH > 7), the production rates decreased again, although it was almost negligible compared to acidic pH. At pH = 11, 10 420 μmol^{-1} and 15 950 μmol^{-1} H_2 were produced over the pure and composite nanotubes, respectively.

The hydrogen production rate was found to be higher with increased amounts of catalysts (Fig. 9d). Over 50 mg of bare and composite nanotubes, 6400 μmol^{-1} and 10 625 μmol^{-1} hydrogen gas were produced *via* aqueous-methanol photoreforming, which was increased to 14 110 and 21 230 μmol^{-1} at 200 mg of catalysts, respectively. However, it can also be seen that the H_2 production rate increases rapidly in the beginning, but as the dose increases, the production rate slows down. Therefore, a slight increase in the H_2 gas production (18 000 to 21 200 μmol^{-1}) was observed after increasing the dose from 100 mg to 200 mg. The main reason for the rate slowing down with increasing dose can be considered to be an increase in

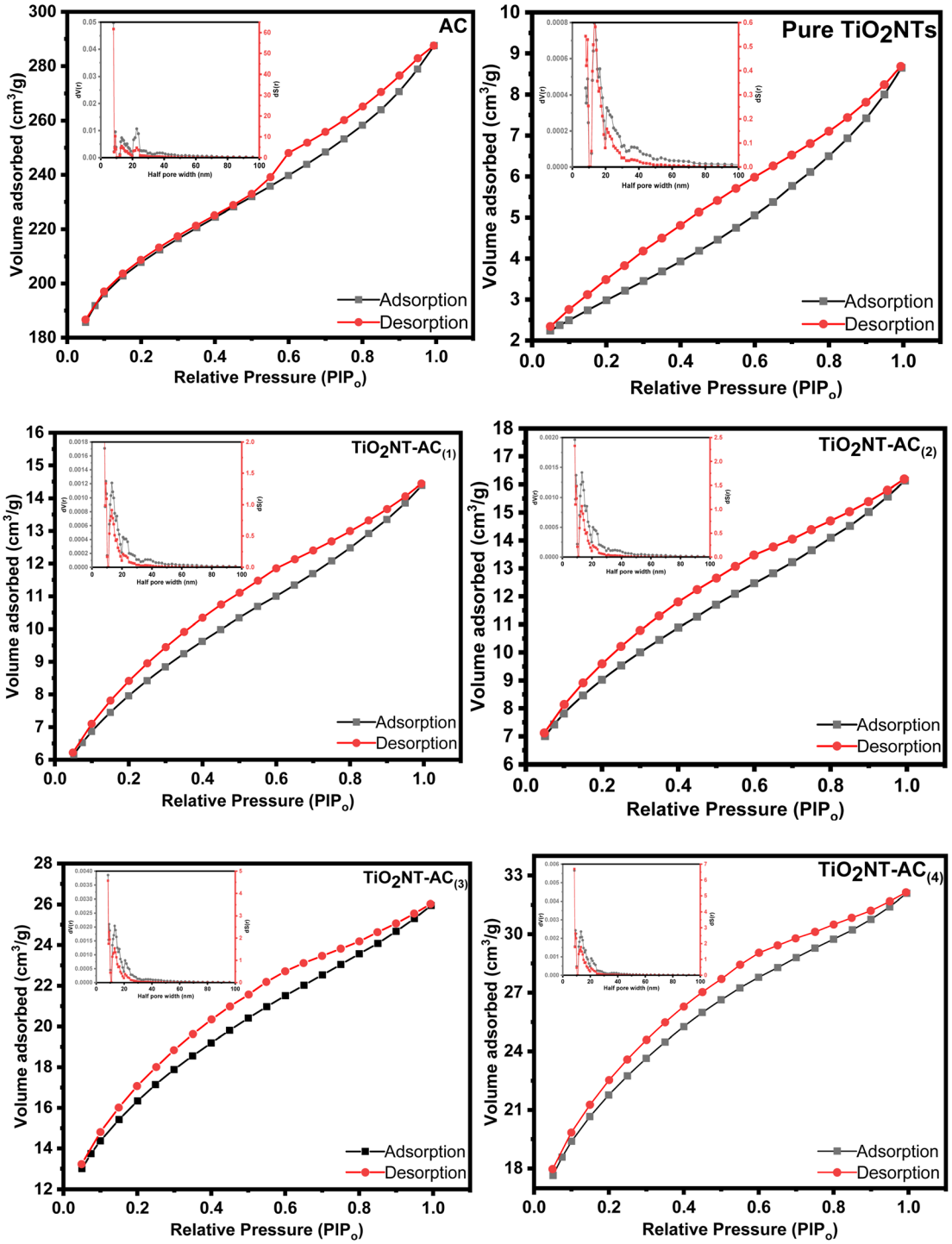

Fig. 8 N_2 adsorption–desorption isotherms and pore size distribution patterns (inset) of the synthesized samples.

light scattering rather than light absorption with increasing dose. Hence, possibly the visible light could not reach the active sites.

The temperature effect (25–55 °C) was also observed in the present study. The hydrogen production rate was found to be higher at the increased temperature (Fig. 9d). Approximately 12 000 μmol^{-1} and 18 000 μmol^{-1} hydrogen gas were produced over pure and composite NTs at 25 °C, which reached up to 13 240 and 22 450 μmol^{-1} at 45 °C, respectively. At a higher temperature (45 °C), only a slight change in the H_2 production was observed for both catalysts. The actual efficiency of any material depends on its reusability. Therefore, reusability also reflects the sustainability of the material. Considering this as the basis, the reusability of composite NTs was also investigated

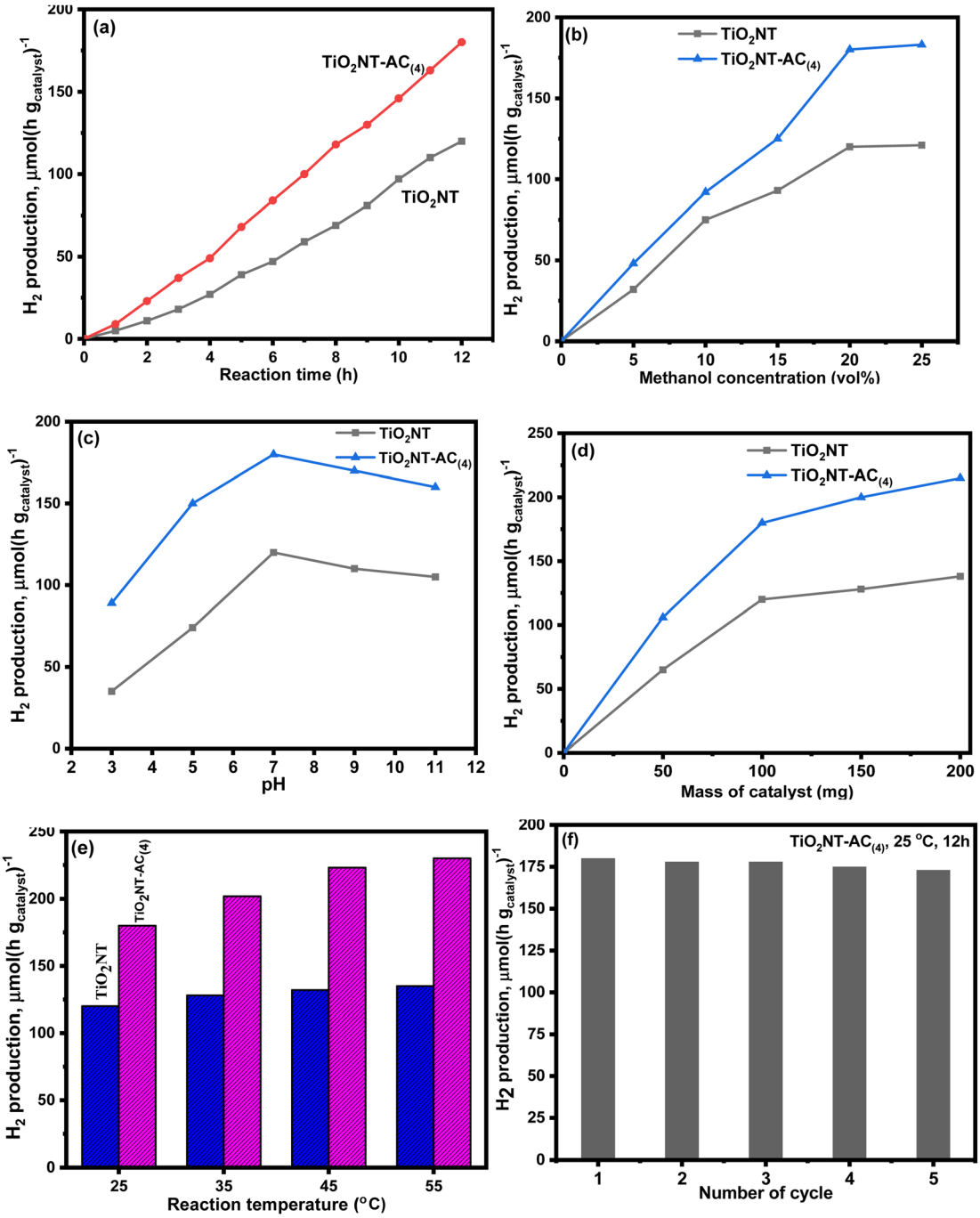

Fig. 9 Photocatalytic hydrogen production over synthesized TiO_2NTs and TiO_2NTs–$AC_{(4)}$ catalysts, (a) effect of reaction time, (b) effect of concentration of methanol, (c) effect of solution pH, (d) effect of mass of catalysts, (e) effect of reaction temperature, and (f) recyclability of the TiO_2NTs–$AC_{(4)}$ catalyst.

in this study. This investigation was carried out for 5 consecutive cycles (Fig. 5f). Before reusing the composite nanotubes, the material was recovered by centrifugation after each cycle; then, it was washed with deionized water and dried by passing N_2 gas. After five cycles, the existing material showed only a slight decline in efficiency, which can be seen in Fig. 5f, so the existing material is useful for many processes. To investigate the structural stability of the catalyst, the XRD pattern of the spent TiO_2NTs–$AC_{(4)}$ catalyst was compared with that of the fresh catalyst. As shown in Fig. 10, the crystal structure of the catalyst was not altered after the reaction; however a slight change in the crystallinity of the sample was observed.

3.10. Plausible reaction mechanism for H_2 production

The whole mechanism of H_2 production can be understood using Scheme 2. When simulated sun light strikes the TiO_2NTs–

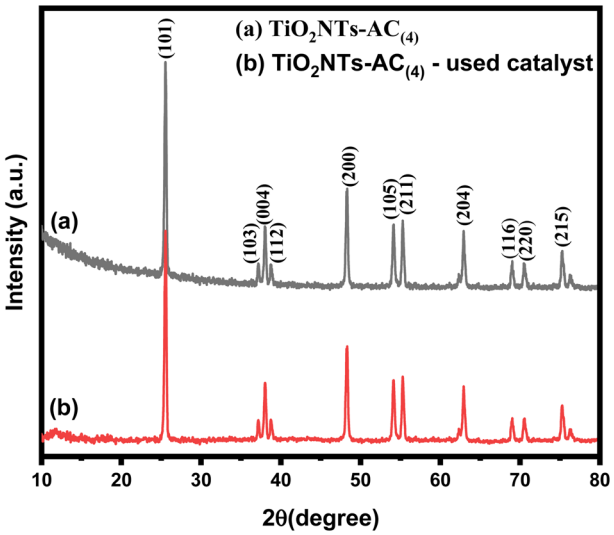

Fig. 10 Comparison of XRD patterns of fresh and spent TiO_2NTs–$AC_{(4)}$ catalysts.

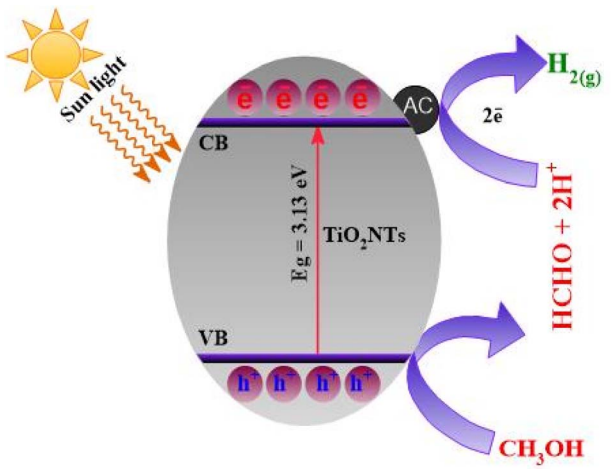

Scheme 2 Plausible reaction mechanism for H_2 production over the TiO_2NTs–AC nanocomposite.

AC composite, holes (h^+) and electrons (e^-) are produced. The AC traps these photogenerated e^- from the CB of TiO_2NTs. This results in the distribution of electric charges across the semiconductor interface, which can prevent the recombination of charge carriers. The produced e^- and h^+ on the surface of TiO_2NTs–AC react with the water and methonal adsorbed on the surface of TiO_2NTs–AC and produce the H_2 gas, as shown in Scheme 2. It should be noted that the sacrificial agents may also serve as proton sources.[5] Therefore, using methanol can be considered for coupling an organic substance's oxidation and proton reduction. To investigate the pathway of photocatalytic reforming of aqueous methanol over the synthesized catalysts, the gaseous products were periodically analyzed using an online gas chromatograph equipped with a TCD and FID. The photocatalytic reformation of aqueous methanol solution mainly produced H_2 in the gas phase and minor quantities of CO, CO_2 and CH_4. At the end of the photocatalytic test, the liquid phase was analyzed using a gas chromatograph equipped with both the FID and MSD. It is observed that methanol undergoes oxidation up to CO_2 through the formation of formaldehyde and formic acid as intermediate species. As previously reported CH_3OH acts as a sacrificial agent and is oxidized by consumption of the photogenerated holes (h^+) in the photocatalyst.[7] The photogenerated electrons (e^-) are then used in the reduction of H^+ to H_2. The presence of activated carbon with TiO_2 decreased the recombination rate of the e^-–h^+ pairs, enhancing the photocatalytic activity of the catalyst.

$$CH_3OH + H_2O + 6h^+ \rightarrow CO_2 + 6H^+ \quad (1)$$

$$2H^+ + 2e^- \rightarrow H_2 \quad (2)$$

A comparison of the photocatalytic activity of the TiO_2NTs–$AC_{(4)}$ catalyst with that of other catalysts reported in the literature is presented in Table 2. The porous TiO_2NTs–$AC_{(4)}$ nanocomposite offered high photocatalytic H_2 rates compared to other TiO_2 containing catalysts such as TiO_2 anatase and TiO_2–AC catalysts. However, the H_2 production rates are higher in the case of few other reported catalysts such as Pt–Cu/TiO_2 catalysts compared to the TiO_2NTs–$AC_{(4)}$ catalyst. It is essential to note

Table 2 Comparison of different photocatalysts reported for H_2 production

S. no.	Photocatalyst	Sacrificial agent	Light source	H_2 production rate	Ref.
1	TiO_2/CuO	Methanol	Xe lamp	8.23 mmol h^{-1} g^{-1}	37
2	AC–TiO_2	Glycerol	Solar light	20 383 μmol g^{-1} h^{-1}	38
3	TiO_2/ACS	Glycerine	Solar light	203 μmol g^{-1} h^{-1}	39
4	PtCu–TiO_2	Methanol	LED irradiation	2383.9 μmol h^{-1}	40
5	Pd–TiO_2	Ethanol	Near-UV light	113 cm^3 STP	16
6	Pd–TiO_2	Ethanol	Visible light	29 cm^3 STP	16
7	Ni/GO–TiO_2	Methanol	UV light	2171 μmol h^{-1} g^{-1}	41
8	CuO/TiO_2NT	Methanol	Mercury lamp	64.2–71.6 mmol h^{-1} g^{-1}	42
9	SnS_2/TiO_2	Methanol	Solar irradiation	195.55 μmol g^{-1}	21
10	Pt–TiO_2	Methanol	UV mercury lamp	38.0 mmol g^{-1} h^{-1}	43
11	TiO_2NTs–AC	Methanol	Solar light	18 000 μmol^{-1} g^{-1} h^{-1}	Present work

that the presence of precious and transition metals and physicochemical characteristics of previously reported catalysts and reaction conditions are different from those of the present work. Moreover, the present research deals with deposition of activated carbon over TiO_2 nanotubes *via* ultrasonication and utilized the synthesized materials for photocatalytic reformation of methanol to produce H_2.

4. Conclusions

In this study, TiO_2 nanotubes are combined with activated carbon derived from biomass to obtain TiO_2NTs–AC nanocomposites. The synthesized materials showed high water-splitting efficiency, under sunlight which proved to be energy efficient for hydrogen production. The synthesized composites are porous in nature (pore volume = 0.020 $cm^3\ g^{-1}$ and half pore width = 8.4 Å) and nanosized (crystallite size = 6.31 nm) with a high surface area (291 $m^2\ g^{-1}$). Its band gap was measured to be 3.15 eV. The prepared material produced approximately 18 000 μmol^{-1} of hydrogen gas using 100 mg of catalyst at pH 7 and 25 °C under 12 hours of continuously simulated sun light irradiation. The material also showed a high reusability rate. Furthermore, the prepared nanocomposite was used for up to 5 cycles without a significant decrease, indicating its good efficiency and sustainability. Furthermore, photocatalytic activity can be influenced by the light absorption, redox nature, and mass transfer of the process, therefore, some more studies are needed to understand the influence of these factors and obtain efficient results. In addition, synthesis of activated carbon needs high energy utilization and release of air pollutants; hence, some more low cost and abundant alternatives can be searched, in the future.

Author contributions

All authors contributed to the study conception and design. Material preparation, data collection and analysis were performed by Shaeel Ahmed Althabaiti Zaheer Khan, Maqsood Ahmad Malik, Salem Mohamed Bawaked, Soad Zahir Al-Sheheri, and Mohamed Mokhtar. The first draft of the manuscript was written by Sharf Ilahi Siddiqui, Maqsood Ahmad Malik, and Katabathini Narasimharao and all authors commented on previous versions of the manuscript. All authors read and approved the final manuscript.

Conflicts of interest

There are no conflicts of interest to declare.

Acknowledgements

The authors extend their appreciation to the Deputyship for Research & Innovation, Ministry of Education in Saudi Arabia for funding this research work through the project number IFPNC-001-130-2020 and Deanship of Scientific Research (DSR), King Abdulaziz University, Jeddah, Saudi Arabia.

References

1 L. Schlapbach and A. Züttel, *Nature*, 2001, **414**, 353–358.
2 J. L. Rowsell and O. M. Yaghi, *Angew. Chem., Int. Ed.*, 2005, **44**, 4670–4679.
3 J. Yang, A. Sudik, C. Wolverton and D. J. Siegel, *Chem. Soc. Rev.*, 2010, **39**, 656–675.
4 S. P. Badwal, S. Giddey and C. Munnings, *Wiley Interdiscip. Rev.: Energy Environ.*, 2013, **2**, 473–487.
5 K. C. Christoforidis and P. Fornasiero, *ChemCatChem*, 2017, **9**, 1523–1544.
6 L. Fan, Z. Tu and S. H. Chan, *Energy Rep.*, 2021, **7**, 8421–8446.
7 J. Wen, J. Xie, X. Chen and X. Li, *Appl. Surf. Sci.*, 2017, **391**, 72–123.
8 T. Shen, H. Xie, B. Gavurová, M. Sangeetha, C. Karthikeyan, T. R. Praveenkumar, C. Xia and S. Manigandan, *Int. J. Hydrogen Energy*, 2023, **48**, 21029–21037.
9 L. Chen, H. Li, H. Wang and K. Liu, *J. Cleaner Prod.*, 2023, 137213.
10 X. Shui, D. Jiang, Y. Li, H. Zhang, J. Yang, X. Zhang and Q. Zhang, *Bioresour. Technol.*, 2023, **367**, 128221.
11 P. Vargas-Ferrer, E. Álvarez-Miranda, C. Tenreiro and F. Jalil-Vega, *J. Cleaner Prod.*, 2023, **409**, 137110.
12 G. Liu, H. Lu, Y. Xu, Q. Quan, H. Lv, X. Cui, J. Chen, L. Jiang and R. J. Behm, *Chem. Eng. J.*, 2023, **455**, 140875.
13 D. Aand, S. Sk, K. Kumar, U. Pal and A. K. Singh, *Int. J. Hydrogen Energy*, 2022, **47**, 7180–7188.
14 J. Talibawo, P. I. Kyesmen, M. C. Cyulinyana and M. Diale, *Nanomaterials*, 2022, **12**, 2961.
15 Q. Cao, S. Hao, Y. Wu, K. Pei, W. You and R. Che, *Chem. Eng. J.*, 2021, **424**, 130444.
16 B. Rusinque, S. Escobedo and H. de Lasa, *Catalysts*, 2021, **11**, 405.
17 G. L. Chiarello, M. V. Dozzi and E. Selli, *J. Energy Chem.*, 2017, **26**, 250–258.
18 J. Yu, L. Qi and M. Jaroniec, *J. Phys. Chem. C*, 2010, **114**, 13118–13125.
19 R. Saravanan, D. Manoj, J. Qin, M. Naushad, F. Gracia, A. F. Lee, M. M. Khan and M. Gracia-Pinilla, *Process Saf. Environ. Prot.*, 2018, **120**, 339–347.
20 D. Xu, Y. Hai, X. Zhang, S. Zhang and R. He, *Appl. Surf. Sci.*, 2017, **400**, 530–536.
21 S. Shanmugaratnam, B. Selvaratnam, A. Baride, R. Koodali, P. Ravirajan, D. Velauthapillai and Y. Shivatharsiny, *Catalysts*, 2021, **11**, 589.
22 H. Song, S. Luo, H. Huang, B. Deng and J. Ye, *ACS Energy Lett.*, 2022, **7**, 1043–1065.
23 A. H. Jawhari, N. Hasan, I. A. Radini, K. Narasimharao and M. A. Malik, *Nanomaterials*, 2022, **12**, 2985.
24 S. A. Althabaiti, M. A. Malik, M. Kumar Khanna, S. M. Bawaked, K. Narasimharao, S. Z. Al-Sheheri, B. Fatima and S. I. Siddiqui, *Nanomaterials*, 2022, **12**, 4472.
25 M. Ouzzine, A. J. Romero-Anaya, M. A. Lillo-Rodenas and A. Linares-Solano, *Carbon*, 2014, **67**, 104–118.
26 M. Asiltürk and Ş. Şener, *Chem. Eng. J.*, 2012, **180**, 354–363.

27 B. Mondol, A. Sarker, A. Shareque, S. C. Dey, M. T. Islam, A. K. Das, S. M. Shamsuddin, M. A. I. Molla and M. Sarker, *Photochem*, 2021, **1**, 54–66.
28 K. Li, H. Ruan, P. Ning, C. Wang, X. Sun, X. Song and S. Han, *Res. Chem. Intermed.*, 2018, **44**, 1209–1233.
29 L. Cui, K. Hui, K. Hui, S. Lee, W. Zhou, Z. Wan and C.-N. H. Thuc, *Mater. Lett.*, 2012, **75**, 175–178.
30 A. H. Jawhari, N. Hasan, I. A. Radini, M. A. Malik and K. Narasimharao, *Fuel*, 2023, **344**, 127998.
31 X.-Y. Liu, M. Huang, H.-L. Ma, Z.-Q. Zhang, J.-M. Gao, Y.-L. Zhu, X.-J. Han and X.-Y. Guo, *Molecules*, 2010, **15**, 7188–7196.
32 Z. Dong, F. Xiao, A. Zhao, L. Liu, T. Sham and Y. Song, *RSC Adv.*, 2016, **6**, 76142–76150.
33 E. Ribeiro, G. Plantard, F. Teyssandier, F. Maury, N. Sadiki, D. Chaumont and V. Goetz, *J. Environ. Chem. Eng.*, 2020, **8**, 104115.
34 Y. G. Alghamdi, B. Krishnakumar, M. A. Malik and S. Alhayyani, *Polymers*, 2022, **14**, 880.
35 S. Muthusamy and J. Charles, *J. Mater. Sci.: Mater. Electron.*, 2021, **32**, 7349–7365.
36 Y. Feng, C. Liu, J. Chen, H. Che, L. Xiao, W. Gu and W. Shi, *RSC Adv.*, 2016, **6**, 38290–38299.
37 J. M. Kum, S. H. Yoo, G. Ali and S. O. Cho, *Int. J. Hydrogen Energy*, 2013, **38**, 13541–13546.
38 N. R. Reddy, U. Bharagav, M. M. Kumari, K. Cheralathan, P. Ojha, M. Shankar and S. W. Joo, *Ceram. Int.*, 2021, **47**, 10216–10225.
39 G. Murali, S. Gopalakrishnan, S. K. Lakhera, B. Neppolian, S. Ponnusamy, S. Harish and M. Navaneethan, *Diamond Relat. Mater.*, 2022, **128**, 109226.
40 H. Wang, H. Qi, X. Sun, S. Jia, X. Li, T. J. Miao, L. Xiong, S. Wang, X. Zhang and X. Liu, *Nat. Mater.*, 2023, 1–8.
41 O. Quiroz-Cardoso, V. Suárez, S. Oros-Ruiz, M. Quintana, S. Ramírez-Rave, M. Suárez-Quezada and R. Gómez, *Top. Catal.*, 2022, **65**, 1015–1027.
42 S. Xu, A. J. Du, J. Liu, J. Ng and D. D. Sun, *Int. J. Hydrogen Energy*, 2011, **36**, 6560–6568.
43 J. Velázquez, R. Fernández-González, L. Díaz, E. P. Melián, V. Rodríguez and P. Núñez, *J. Alloys Compd.*, 2017, **721**, 405–410.